Journal of Solar Energy Research (JSER)

Journal homepage: jser.ut.ac.ir

Solar microgrids fast and accurate fault detection, location and classification strategy using on-line phaselet, current injection kits', traveling-waves, and mathematical morphology

Mostafa Dodangeh, Navid Ghaffarzadeh*

Faculty of Technical and Engineering, Imam Khomeini International University, Qazvin, Iran
Received: 2020-10-05
Accepted: 2021-05-16

A B S T RAC T

In this paper, a new fast and accurate method for fault detection, location and classification on multi-terminal direct current (MTDC) distribution networks connected to solar distributed generation and loads presented. Some issues such as DC resources and loads expanding, and try to the power quality increasing have led to MTDC networks' development. It is important to recognize the fault type in order to continue service and prevent further damages. In this method, a circuit kit is connected to the network. Fault detection is performed with the measurement of the current of the connected kits and the traveling-waves of the fault current and applying it to a mathematical morphology filter, in the Fault time. Determine the type and location of faults using a mathematical morphology filter, circuit equations and current calculations. DC series and ground arc faults are considered as DC distribution network disturbances. The presented method was tested in a solar DC network connected to energy storages and solar resources with many faults. The results illustrate the validity of the proposed method. The main advantages of the proposed fault location and classification strategy are higher speed and accuracy than conventional approaches. The fault location error of the presented algorithm is less than 6.5 percent in the worst case. This method robustly operates to changing in sampling frequency [0.5-50 KHz], fault resistance [0.005-120 Ohm], and works very well in high impedance fault.

Keywords:
MTDC solar network, fault detection and classification, mathematical morphology, current injection kit, on-line phaselet

1. Introduction

The rapid and accurate detection, location and classification of the fault are highly effective in developing the reliability indexes, diminishing expected energy not supply, and increasing the speed of network recovery and reconstruction. Growing DC consumption in distribution networks, connecting photovoltaic resources to the network, trying to enhance the power quality and responding to further loads has expanded MTDC solar networks. And the other hand, power electronic converters usage improves the capacity, quality, size, weight, and equipment consumption and the load flow on the MTDC networks.

* Corresponding Author's Email: ghaffarzadeh@eng.ikiu.ac.ir

The implementation of conventional schemes for fault detection and location on MTDC networks has some problems. The accuracy of impedance-based methods is not sufficient at power frequency for distribution networks. Traditional protection methods that are based on undervoltage/overcurrent [1, 2], rate of change in current/voltage [3], or either lack the required sensitivity for detecting high-resistance faults, or are Unreliable to communication delay and failure. Passive-Overcurrent protection based on discrete wavelet transform is proposed to different types of faults detection and classification [1, 4]. Yet, none of the above schemes meet the speed required for an MTDC solar network [2], [4]. In [5], a directional current-based protection scheme is proposed for low voltage dc (LVDC) grids. However, apart from these schemes' unreliability to communication fails, the operation of high bandwidth fiber optic communication is expensive and not excusable for LVDC grids.

The protection challenges of the solar and wind networks analyzed in [6]. A novel fault detection, characterization, and fault current control algorithm for a standalone solar-photovoltaic (PV) based DC microgrids presented in [7]. A distributed incremental adaptive filter (DIAF) controlled utility interfaced photovoltaic (PV) - battery microgrid system is presented with power quality features [8]. In [8-16], Solar DC microgrids control and management methods and voltage stability are presented.

Traveling waves based methods have been used widely to detect transmission line faults [17, 18]. Methods based on traveling waves and time-domain analysis are used in HVDC networks [19]. In some methods, Wavelet has been mixed with other techniques such as artificial neural networks, fuzzy logic increases the performance of the proposed protection algorithm [17-24]. Some of these methods depend on the location of the fault and the arrival time of the traveling waves [25]. Determination of the fault location in the MTDC distribution grids should be done with high accuracy and sureness due to multiple and longitudinal splits and branches. In [26, 27], a DC bus protection scheme in DC distribution grids have been suggested. The actual impedance approximation method is used in a network. Detection of voltage drop in DC microgrid is provided using the power probe unit proposed [1, 28, 29]. Few power electronics converter-based power probe units for injecting AC signals are in [26, 30-33]. The simple solar network or single-bus solar microgrids investigated in most of the mentioned researches. In this paper, a high-precision and high-speed method is proposed to fault determination, location and classification in multi terminal DC solar distribution networks using current injection, mathematical morphology, and online phaselet. Using the traveling waves derived from the online phaselet transform and mathematical morphology, the fault occurrence and its type are identified. The attenuation factor (γ) is calculated based on the sampling of the fault current in the interconnected multi-bus solar system. This method was tested on an MTDC solar network with many faults. The results illustrate the validation of the proposed method.

2. Method

2.1 Current injection technique

By adjoining the Cq branch to the current injection kit provided in[34], part of the switching current passing through this branch and reduces the switching losses and reduces the error of fault locating in the line close in fault. Figure 1 illustrates the proposed kit. The optimum value of Cq is selected by considering the total loss of switching, the cost of capacitors installing, and reactive losses. The kit that be shown in figure 1 connected to the MTDC network buses. Figure 2 illustrate the equivalent circuit of the faulted network and the kit in the fault time. If the fault does not occur, the current does not pass through the connected kits.

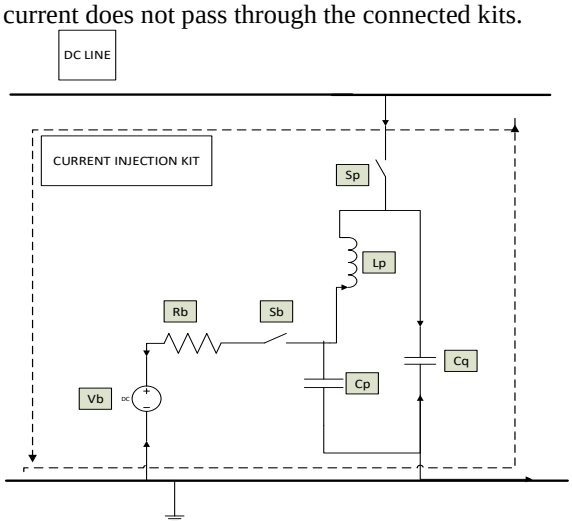

Figure 1 Proposed current injection kit

The equation of the current of the faulted part of the grid is 1 and 2.

$$\frac{d^2 i_p(t)}{dt^2} + \frac{R}{L}\frac{di_p(t)}{dt} + \frac{1}{LC} i_p(t) = 0 \quad (1)$$

$$i_p(t) = K_1 e^{-\gamma t}\sin(\omega_d t) + K_2 e^{-\gamma t}\cos(\omega_d t) \quad (2)$$

Such that

$$\omega_d^2 = \omega_n^2 - \gamma^2$$

$$\gamma = \frac{R}{2L}$$

$$\omega_n = \sqrt{\frac{L_d + C_q}{C_q C_p (L_d + L_p) + C_p L_d L_p}}$$

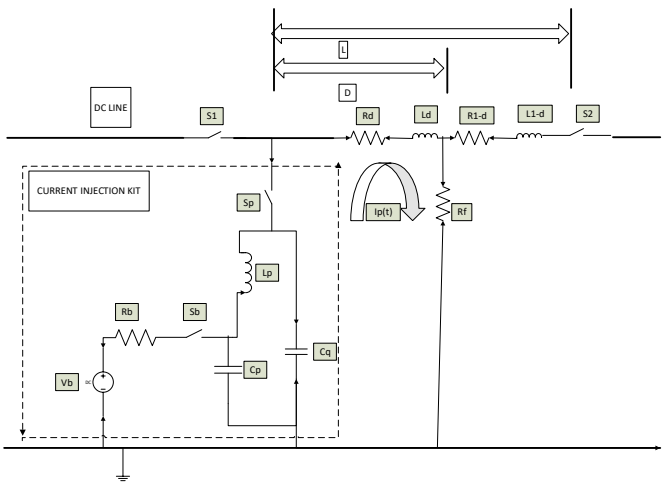

Figure 2 Equivalent circuit of the faulted network and the kit

Due to the line impedance-to-length dependence, the natural frequency (ω_n) of fault current calculates by 3.

$$\omega_n = \sqrt{\frac{L_u d + C_q}{C_q C_p (L_u d + L_p) + C_p L_u d L_p}} \quad (3)$$

Thus, the location of the occurred fault is calculated using 4 and the error percent of the estimation of fault's location is calculated by 5.

$$d = \frac{C_q - C_p L_p C_q \omega_n^2}{L_u (C_p (L_p + C_q)\omega_n^2 - 1)} \quad (4)$$

$$= \frac{C_q - C_p L_p C_q (\omega_d^2 + \gamma^2)}{L_u (C_p (L_p + C_q)(\omega_d^2 + \gamma^2) - 1)}$$

$$\varepsilon = \left| \frac{d_{cal} - d_{act}}{d_{act}} \right| \times 100 \quad (5)$$

The equation of the curve of the fault current is 6, and by two samples of the fault current, the attenuation factor γ is calculated by (7).

$$i_{p^p}(t) = K e^{-\gamma t} \quad (6)$$

$$\gamma_n = \frac{\ln(i_n) - \ln(i_n + 1)}{t_{n+1} - t_n} \quad (7)$$

2.2 Online phaselet transform

The wavelet transform holds the correlation between the frequency and time of the signal and is a very good ability at the time-frequency resolution. This feature of the wavelet transform can be used to determine the arrival time of the traveling wave and its following reflections. It is well known that discrete wavelet transform (DWT) is operated to different sampled (digitized) signals, to show their time-scale representation. The phaselet transform is a shift invariant wavelet transform. The mother phaselet is the mother wavelet multiply to a phase shifter functions. To execute this transform, the primary signal is passed into a band-pass filter (G is named mother phaselet) to give a detail part, for the first level. At the same level, and by convolving the signal with a low-pass filter (H), results in an approximate component. G and H are orthogonal vectors with N ×1 elements [26]. For the second level, the approximate component is down-sampled by two, i.e. its samples are halved, and then are passed into G and H to give the next level approximate and detail components, respectively at this level. Continuing this algorithm to the ith level, makes the original signal to be decomposed to i detail components and an approximate one. This scheme is presented in Figure 3 up to four decomposition levels.

To present the above description in a mathematical form, for the ith level of decomposition, the detail, and approximate signals may be obtained as equations 8 and 9.

$$A_i = A_{i-1} \times G \quad (8)$$

$$D_i = A_{i-1} \times H \quad (9)$$

According to the aforementioned descriptions, in order to find the ith level detail component, a serial process must be done through successive

convolutions of approximate components with band-pass and low-pass filters up to the wanted decomposition level.

In on-line usages of DWT/DPT, this successive manner, which is time-delay, is not justifiable. In these applications, some detail or approximate components at some predefined frequency bands (various levels of decomposition) must be inspected. But, according to equations 8 and 9, the elements of the components in the ith level cannot be computed unless the approximate component of the (i-1) th level is fully finished, and the latter cannot be defined unless the computations of the previous level are finalized. Consequently, the monitoring or inspecting mission cannot be produced, unless through a successive method. In this section, a digital filter for on-line applications of DPT is formed. The first feature of this filter is that the kth element of D1 or A1 comes out along with the kth element of all of the upper-level detail or approximate components. Let equation (1) and (2) with i= 2 to be rewritten as equations 10 and 11.

$$G_j = H_{ii} G_{i-1} = \left(\prod_{m=2}^{i} H_{mm}\right) \times G \quad 12$$

$$A_j = X \times G \wedge i \quad 13$$

$$D_j = X \times G_i \quad 14$$

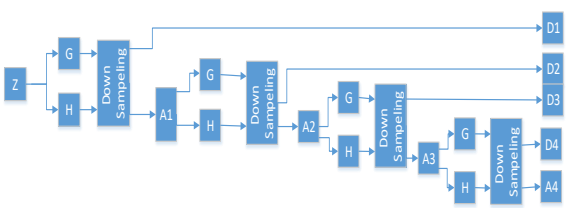

Figure 3 Four decomposition levels of main signal Z by DPT

$$A_2 = A_1 \times G = X \times G \times G \quad 10$$

$$D_2 = D_1 \times G = X \times G \times H \quad 11$$

Therefore

In the same way, the matrix for generating the elements of online approximate components can be introduced[35].

2.3 Mathematical morphology filter

Mathematical morphology in the field of time and with brief information windows examines the appearance of high-frequency signals. The erosion(f_e) and dilation(f_d) of the F input signal with the domain Df and the structural element S with the domain D_S are defined as 15 and 16. And using the dilation and erosion the close(f_c) and open(f_o) relations are defined as 17 and 18, and the morphological filter is defined according to the four relations that have been introduced in the form of equation 19.

The equation 19 filter operates at high accuracy in detecting the range of disturbances but is incapable of detecting the direction of the disturbance signal. This problem is resolved by using equation 20.

$$f_e(k) = (f \ ! \ s)(k) = \max\{f(k+l) - s(l)\} \quad 15$$

$$f_d(k) = (f \oplus s)(k) = \max\{f(k-l) + s(l)\} \quad 16$$

$$f_c(k) = (f \ . s)(k) = ((f \ ! \ s) \oplus s)(k) \quad 17$$

$$f_o(k) = (f \circ s)(k) = ((f \oplus s) \ ! \ s)(k) \quad 18$$

$$MF(k) = \frac{(f(k) \, o \, (f \ . s)(k))}{2} + \frac{(f(k).(f \ o \, s)(k))}{2} \quad 19$$

$k \varepsilon D_f$ and $l \varepsilon D_s$ Such that

$$D_f = \{0,1,2,...,K-1\}$$

$$D_s = \{0,1,2,...,L-1\}$$

Based on [32-34], when the erosion signal lags the dilation signal, the MMF output has a positive pole; when the erosion signal leads the dilation signal, the MMF output has a negative pole. Also, when there is no sudden change in the initial signal, there isn't the phase difference between the erosion and dilation signals and the MMF output is zero.

With applying the online phaselet to the disturbance signal in MTDC distribution networks, traveling waves is obtained.

By applying the traveling wave of the fault current signal to the morphological filter, for various types of fault, faults type is detected. Many types of faults are simulated in the Cigre benchmark MTDC solar network and the accuracy of the proposed method is

validated in part 3. The proposed method's Flowchart is shown in figure 4.

3. Simulation results

In order to examine the proposed method, a multi-terminal DC solar distribution network was simulated in PSCAD/EMTDC software. This network includes cable and overhead lines and connected to the power grid and several solar distributed generation and loads. Loads include electrical vehicle stations, agriculture electrical vehicle and other public and commercials loads. Distributed generation include photovoltaic farm, solar houses and parking. Figure 5 illustrates this solar network. Different types of faults were simulated with different conditions in terms of the location of faults, arc's resistance, and type of faults.

$$MMF(k)=\begin{cases} MF_d(k)-MF_e(k) \Leftrightarrow MF_d(k-1)<MF_d(k) \\ MF_e(k)-MF_d(k) \Leftrightarrow MF_e(k-1)<MF_e(k) \end{cases} \quad (20)$$

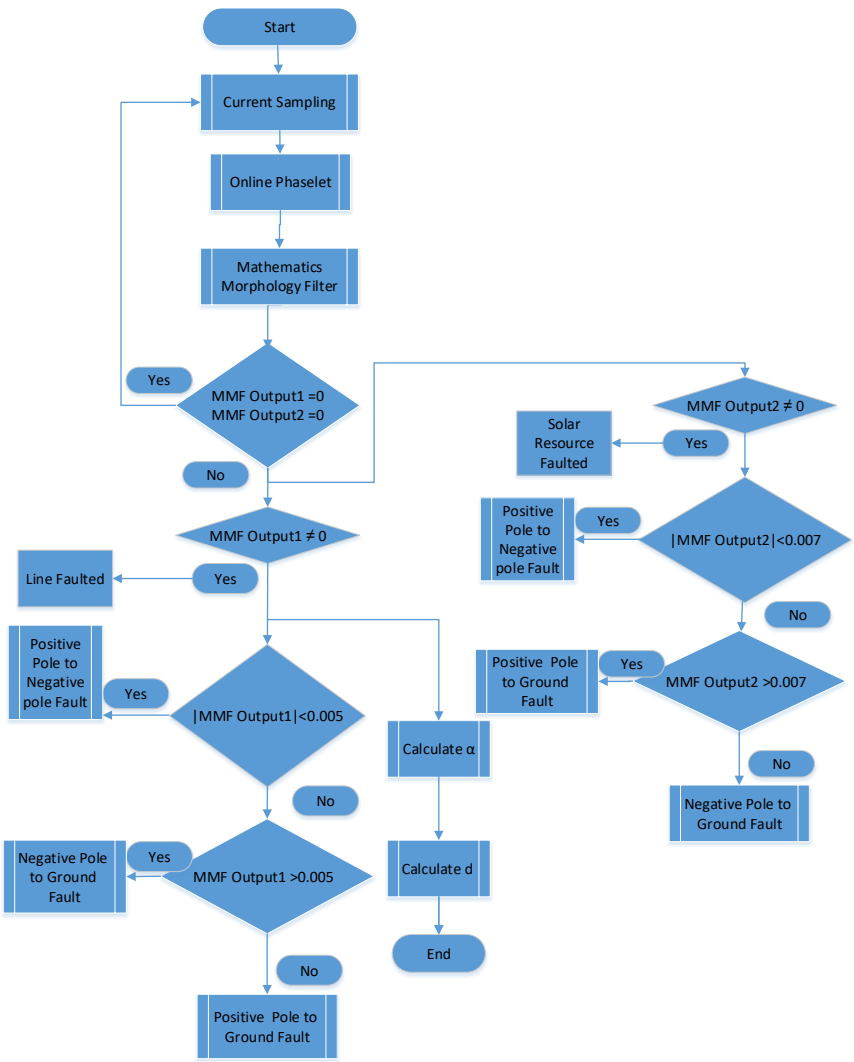

Figure 4 Proposed method flowchart

Fault current signals were measured in all mode. In each case, two samples used to calculate the fault current attenuation factor. Using the phaslet transform, traveling waves was calculated from fault current. The resulted waves applied to the mathematical morphology filter and the type of faults was determined for different situations with high precision. Determine the fault location in lines faulted cases using equation 4 and the fault location error percent calculated in lines faulted cases by formula 5. Results of some of the lines faults simulations are presented in Table 1. Results of some of the solar resources faults simulations are presented in Table 2.

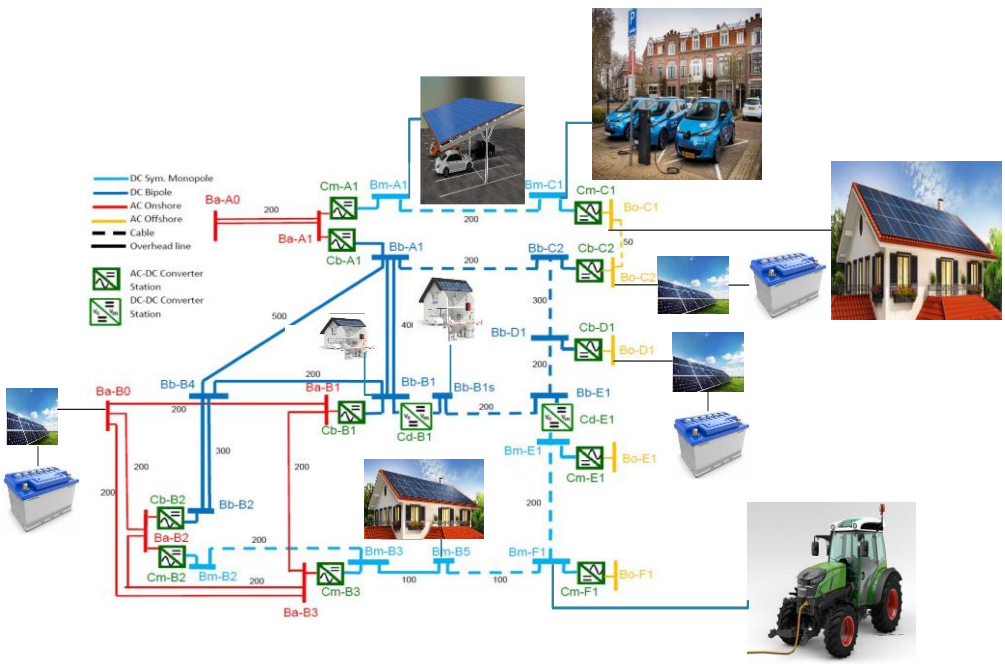

Figure 5 Multi terminal direct current solar Test network

Table1 Fault location and classification method's results in lines faulted cases

No.	Fault			Fault resistance	PN fault			PG fault			NG fault		
	Beginning of Line	End of line	Actual fault distance(%)		Calculated fault distance(%)	Fault location error (%)	Fault type	Calculated fault distance(%)	Fault location error (%)	Fault type	Calculated fault distance(%)	Fault location error (%)	Fault type
1	Bb-D1	Bb-E1	10	5	10.09	0.9	PN	10	0	PG	9.92	0.8	NG
2	Bm-B5	Bm-B3	95	50	95.5	0.526	PN	95.64	0.6736	PG	95.95	1	NG
3	Bm-B2	Bm-B3	65	50	65.31	0.4769	PN	65.47	0. 7231	PG	65.27	0.4154	NG
4	Bb-B4	Bb-A1	30	0.05	30.22	0.7333	PN	30	0	PG	30.19	0.633	NG
5	Bb-B1	Bb-B4	5	0.05	4.98	0. 4	PN	4.977	0.46	PG	4.984	0.32	NG
6	Bb-C2	Bb-A1	5	0.05	4.97	0.6	PN	4.981	0.38	PG	4.978	0.44	NG

7	*Bb-A1*	*Bb-B4*	*15*	*0.05*	*14.98*	*0.1333*	*PN*	*15*	*0*	*PG*	*14.97*	*0.1533*	*NG*
8	*Bm-A1*	*Bm-C1*	*5*	*50*	*5.025*	*0.5*	*PN*	*5.043*	*0.86*	*PG*	*5.0099*	*0.198*	*NG*
9	*Bb-D1*	*Bb-C2*	*10*	*50*	*10.071*	*0.71*	*PN*	*10.056*	*0.56*	*PG*	*10.049*	*0.49*	*NG*
10	*Bm-F1*	*Bm-E1*	*35*	*50*	*35*	*0*	*PN*	*35.18*	*0.5143*	*PG*	*35.2*	*0.5714*	*NG*
11	*Bm-F1*	*Bm-B5*	*60*	*5*	*60*	*0*	*PN*	*60.18*	*0.30*	*PG*	*60.08*	*0.133*	*NG*
12	*Bb-B1*	*Bb-A1*	*30*	*50*	*30.04*	*0.1333*	*PN*	*30.042*	*0.14*	*PG*	*30.026*	*0.8666*	*NG*
13	*Bm-B3*	*Bm-B2*	*99*	*0.05*	*99.2*	*0.0202*	*PN*	*98.9*	*0.0101*	*PG*	*99.8*	*0.808*	*NG*
14	*Bb-B1*	*Bb-A1*	*45*	*0.05*	*45.04*	*0.08889*	*PN*	*44.989*	*0.02444*	*PG*	*45*	*0*	*NG*
15	*Bb-E1*	*Bb-D1*	*40*	*0.05*	*40*	*0*	*PN*	*39.89*	*0.275*	*PG*	*40*	*0*	*NG*
16	*Bm-C1*	*Bm-A1*	*80*	*0.05*	*79.96*	*0.05*	*PN*	*80*	*0*	*PG*	*80*	*0*	*NG*
17	*Bb-C2*	*Bb-D1*	*50*	*5*	*50.11*	*0.22*	*PN*	*50.3*	*0.6*	*PG*	*50.24*	*0.48*	*NG*
18	*Bb-B4*	*Bb-B1*	*5*	*50*	*4.98*	*0.4*	*PN*	*5.3*	*0.6*	*PG*	*5.015*	*0.3*	*NG*
19	*Bm-E1*	*Bm-F1*	*15*	*50*	*14.95*	*0.3333*	*PN*	*15.011*	*0.07333*	*PG*	*15.031*	*0.2067*	*NG*
20	*Bm-B3*	*Bm-B5*	*55*	*0.05*	*55.11*	*0.2*	*PN*	*54.907*	*0.1691*	*PG*	*55.031*	*0.05636*	*NG*
21	*Bm-F1*	*Bm-E1*	*5*	*5*	*70*	*0*	*PN*	*70.322*	*0.46*	*PG*	*69.989*	*0.0157*	*NG*
22	*Bb-B1s*	*Bb-E1*	*30*	*0.05*	*30.22*	*0.7333*	*PN*	*30*	*0*	*PG*	*30.19*	*0.633*	*NG*
23	*Bb-B4*	*Bb-B1*	*25*	*0.05*	*25.11*	*0.44*	*PN*	*24.81*	*0.76*	*PG*	*24.991*	*0.036*	*NG*
24	*Bb-B4*	*Bb-A1*	*45*	*0.05*	*44.86*	*0.3111*	*PN*	*45.21*	*0.4667*	*PG*	*45*	*0*	*NG*
25	*Bb-B2*	*Bb-B4*	*40*	*5*	*40.01*	*0.775*	*PN*	*40.07*	*0.175*	*PG*	*39.86*	*0.35*	*NG*
26	*Bb-A1*	*Bb-B1*	*85*	*5*	*85.29*	*0.3412*	*PN*	*85.2*	*0.2353*	*PG*	*85.18*	*0.2118*	*NG*
27	*Bb-B1s*	*Bb-E1*	*5*	*50*	*5.025*	*0.5*	*PN*	*5.023*	*0.46*	*PG*	*5.016*	*0.32*	*NG*
23	*Bb-B4*	*Bb-B1*	*85*	*25*	*85.29*	*0.3412*	*PN*	*85.2*	*0.2353*	*PG*	*85.18*	*0.2118*	*NG*
24	*Bb-D1*	*Bb-C2*	*35*	*25*	*35.18*	*0.5143*	*PN*	*35.27*	*0.771*	*PG*	*35.2*	*0.5714*	*NG*
25	*Bb-D1*	*Bb-C2*	*5*	*25*	*70*	*0*	*PN*	*70.322*	*0.46*	*PG*	*69.989*	*0.0157*	*NG*
26	*Bm-B2*	*Bm-B3*	*55*	*25*	*55.11*	*0.2*	*PN*	*54.907*	*0.1691*	*PG*	*55.031*	*0.05636*	*NG*
27	*Bm-B3*	*Bm-B5*	*55*	*25*	*55.22*	*0.4*	*PN*	*54.031*	*0.05636*	*PG*	*55.907*	*0.1691*	*NG*

28	Bm-B2	Bm-B3	65	30	65.27	0.4154	PN	65.31	0.4769	PG	65.47	0.7231	NG
29	Bb-B1	Bb-B4	30	25	30.22	0.7333	PN	30	0	PG	30.19	0.633	NG
30	Bm-B2	Bm-B3	5	30	70	0	PN	70.322	0.46	PG	69.989	0.0157	NG
31	Bb-B4	Bb-A1	99	30	98.9	0.0101	PN	99.8	0.808	PG	99.2	0.0202	NG
32	Bb-E1	Bb-D1	40	50	39.89	0.275	PN	40	0	PG	10.11	0.275	NG
33	Bm-B3	Bm-B2	30	30	30.042	0.14	PN	30.026	0.8666	PG	30.04	0.1333	NG
34	Bb-B1	Bb-A1	10	5	10.09	0.9	PN	10	0	PG	9.92	0.8	NG
35	Bb-E1	Bb-D1	45	30	44.96	0.08889	PN	44.989	0.02444	PG	45.04	0.08889	NG

Table2 Fault classification method results in solar resources faulted cases

No.	**Bus**	**Applied Fault**		**PN**	**PG**	**NG**
		Bus type	*Resistance*	**Detected Fault type**		
1	Bo-D1	Source	0.005 & 5	PN	PG	NG
2	Ba-B0	Source	0.005 & 25	PN	PG	NG
3	Bm-B5	Source	10 & 25	PN	PG	NG
4	Bo-C2	Source	0.005 & 25	PN	PG	NG
5	Bm-A1	Source	10 & 25	PN	PG	NG
6	Bo-D1	Source	10 & 25	PN	PG	NG
7	Ba-B0	Source	5 & 15	PN	PG	NG
8	Bm-B5	Source	0.005 & 5	PN	PG	NG
9	Bo-C2	Source	5 & 15	PN	PG	NG
10	Bm-A1	Source	0.005 & 5	PN	PG	NG
11	Bo-D1	Source	8 & 20	PN	PG	NG
12	Ba-B0	Source	8 & 20	PN	PG	NG
13	Bm-B5	Source	8 & 20	PN	PG	NG
14	Bo-C2	Source	8 & 20	PN	PG	NG
15	Bm-A1	Source	8 & 20	PN	PG	NG

Three types of faults were applied, with the distance of 60% of the length of the line between the bus Bb-E1 and the bus Bb-B4 and among the fault's resistance equal to 15 ohms, including positive pole to the ground, negative pole to the ground and positive pole to negative pole. Fault currents were measured in three modes. Figure 6-a and Figure 7-a shows the fault currents in each type of operated fault.

The three-mode phaselets of fault currents were calculated, using online phaselet and db4 as mother wavelet with shift invariant phase zero degree for lines faults, 30 degrees for solar resources faults. Application of online phaselet has increased the speed of fault detection and fault classification. Figure 6-**b** and Figure 7-b illustrates its diagrams.

Figure 6-c and Figure 7-c shows the output of the mathematical morphology filter for three types of faults. Depending on the diagrams of Figure 6-c, the proposed method operates with high accuracy and speed to detect types of faults.

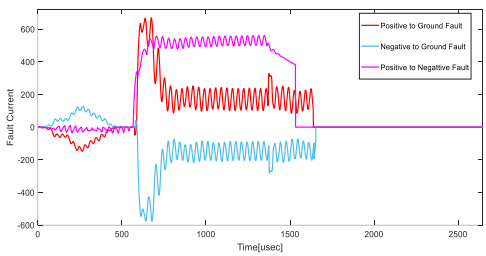

a

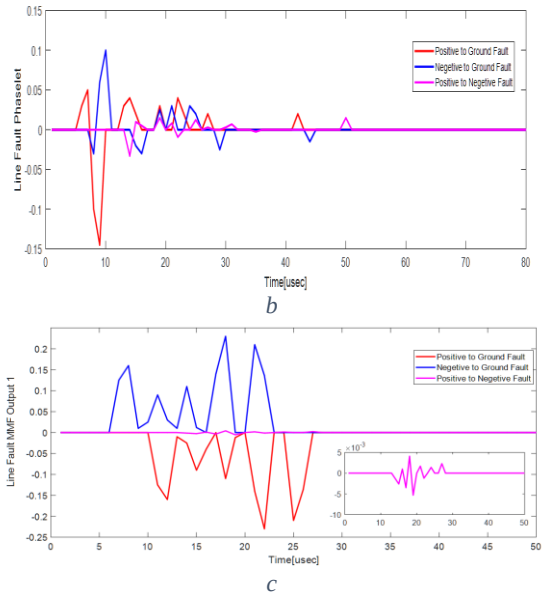

Figure 6 Line faults signals

6-a: Fault current in three modes ،6-b :online phaselet output of fault current, 6-c :mathematical morphology filters out put

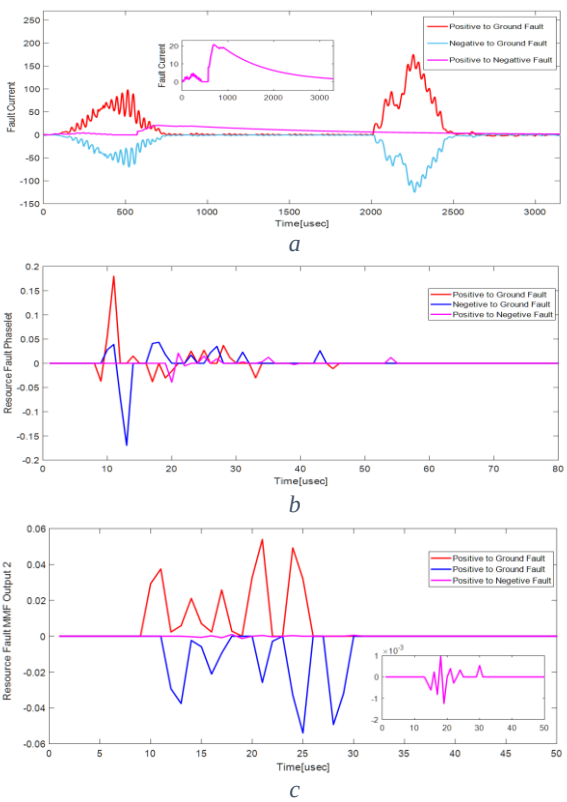

Figure 7 Source faults signals

7-a: Fault current in three modes, 7-b :online phaselet output of fault current, 7-c :mathematical morphology filters out put

4. Classification criteria Selection

2500 various faults evaluated on the MTDC solar network with different conditions of arc resistance, sampling frequency, location, and type of faults. Some of which are presented in tables 1, 2, and 3. The value of the mathematical morphology filter output of all line faulted cases given in Figure 8 and solar resource faulted cases is shown in Figure 9.

According to various line faults conditions simulations, the fault classification criterion was considered equal to ±0.005 for line faults MMF output 1.

The various sources faults applied to microgrid and by attention to results, ±0.007 for solar generation faults MMF output 2. Faults classify properly with selected thresholds according to Figure 8 and Figure 9.

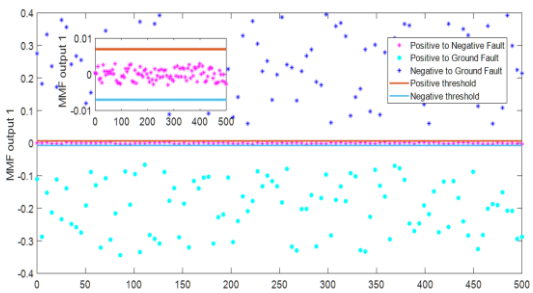

Figure 8 Value of the mathematical morphology filter output of various line faults

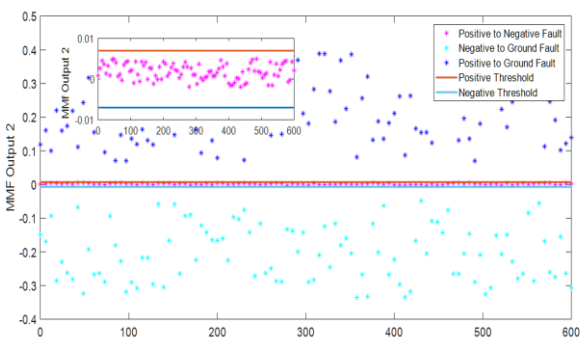

Figure 9 Value of the mathematical morphology filter output of various resources faults

5. The fault resistance effect on the proposed fault location method

By adding the Cq branch to the flow injection kit presented in [34]and installing the kits, the proposed fault location method was used to determine the fault location. Also, the error of the fault location was significantly reduced compared to the presented method in [34] for faults near the beginning of the line (close in fault) with high fault resistance. The error of the method presented in [34] is shown in Figure 10. By applying different faults along the line and with variable values of arc resistance from zero to 120 ohms using the proposed method, the location of the occurrence for all types of fault is calculated. Figure 11 Illustrate the average error of the three types of fault by the proposed fault location method.

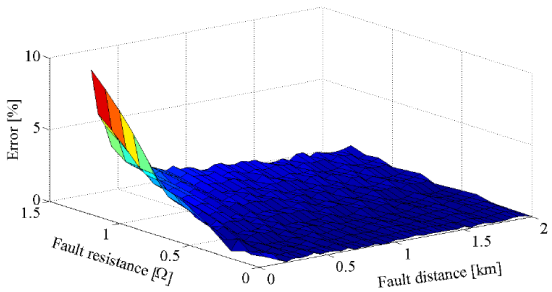

Figure 10 error of the method presented in [34]

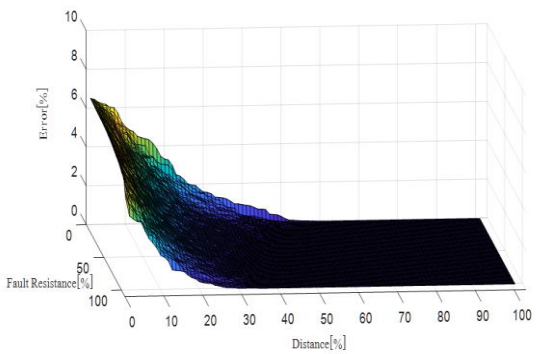

Figure 11 error of the presented method

According to Figure 11 and the results of Table 1, the proposed method has a good response to the impedance fault. Faults with 120-ohm resistance applied at various points along the line length and the fault location calculated using the proposed method.

The maximum of the fault location error is less than 6.5%. According to the above mentioned, this method is robust to high impedance fault.

6. Sampling Frequency Effect

The proposed method was used by different sampling frequency from 500Hz to 50KHz, and the results of 0.5, 1, 2, 10, 20, 30, 40, and 50KHz sampling frequencies given in Table 3. Furthermore, the arc resistance and applied fault location changed to determine the effect of sampling frequency variation in the different fault cases and conditions.

The results of Table 3 clearly show that changing the sampling frequency in a wide range does not change the efficiency and accuracy of the proposed method in the fault locating. For each fault types using the proposed method, the fault location was computed with very lowly error.

Table 3 Results of fault location method with various sampling frequency

Sampling frequency	Actual fault distance (%)	5	5	25	30	45	60	85	95
	Fault resistance	5	0.05	25	25	5	25	0.05	5
500 Hz	Estimated fault distance (%)	4.992	4.99	25.1236	30.03	44.986	60	85.58	94.71
	Fault location error (%)	0.16	0.2	0.4944	0.1	0.0311	0	0.683	0.3053
1 kHz	Estimated fault distance (%)	5.09	4.99	25.19	30.15	45	60.7	84.6	95.8
	Fault location error (%)	0.18	0.2	0.76	0.5	0	1.167	0.47	0.842
2 kHz	Estimated fault distance (%)	5	5.037	25.15	30	44.972	60.156	85. 9	95
	Fault location error (%)	0	0.74	0.6	0	0.06223	0.26	0.9412	0
5 kHz	Estimated fault distance (%)	5.017	4.995	24.4	29.99	45.2	59.69	85.2	95
	Fault location error (%)	0.34	0.1	0.24	0.03334	0.44445	0.5167	0.2352	0
10 kHz	Estimated fault distance (%)	4.991	5.019	25.09	29.89	45	60.8	85.09	94.62
	Fault location error (%)	0.18	0.38	0.36	0.3667	0	1.334	0.10588	0.3984
20 kHz	Estimated fault distance (%)	5.012	4.994	25.145	29.93	44.79	60	85.1	94.54
	Fault location error (%)	0.24	0.12	0.592	0.2334	0.4667	0	0.1176	0.4842
30 kHz	Estimated fault distance (%)	4.99	4.96	25.2	30.09	44.7	60.1	84.4	95.54
	Fault location error (%)	0.2	0.8	0.8	0.3	0.667	0.1667	0.706	0.4632
40 kHz	Estimated fault distance (%)	4.991	5	24.94	30.1	45	59.8	84.6	95.19
	Fault location error (%)	0.18	0	0.24	0.334	0	0.3334	0.47	0.2
50 kHz	Estimated fault distance (%)	5.001	5	25.1	30.057	45.04	59.7	85.18	95.7
	Fault location error (%)	0.02	0	0.4	0.1899	0.0889	0.5	0.2118	0.737

7. Conclusion

In this paper, a new method of fault detection and fault location in MTDC solar networks is proposed which can be used to detect and classify line faults and solar resources faults fast, accurate, and efficiently in MTDC solar microgrids. The occurred fault location is determinate exactly by connecting a kit to the solar microgrid. Using the proposed kit diminishes the fault location error, especially the faults that occurred at the line beginning and near the kit. In fault occurrence, fault detection is done with measurement of traveling waves of fault current by online phaselet and applying to a mathematical morphology filter. The fault type classification is done according to the mathematical morphology filter amount. The line faults distance determines using the circuit equations and current calculations. The accuracy of the presented method in an MTDC solar system was tested with various faults in terms of type, location, resistance, and sampling frequencies. The proposed approach is robust to sampling frequency change and Arc resistance fluctuations. The proposed method works with excellent performance in high impedance faults. More importantly, the proposed approach works properly for any MTDC solar network, irrespective of the grid's topology, that is, the number of network's radial lines, meshes, nodes, and rings.

Acknowledgments

The authors would like to thank Imam Khomeini International University for its financial support of this project.

Appendix

Nomenclature

R	*Equivalent resistance of the KIT and faulted part of the grid*
L	*Equivalent inductance of the KIT and faulted part of the grid*
C	*Equivalent capacitance of the KIT and faulted part of the grid*
i_p	*Current of the faulted part of the grid*
d	*Distance of fault location*
Cp , Cq	*Capacitors of the KIT*
S_b , S_p	*switches of the KIT*
L_p	*Inductance of the KIT*
V_b , R_b	*Battery voltage and resistance of the Kit*
ω_n	*The natural frequency*
γ	*The attenuation factor*
NG	*Negative pole to ground fault*
PG	*Positive pole to ground fault*
PN	*Positive pole to negative pole fault*
f_d	*Dilation of signals*
f_e	*Erosion of signals*
f_c	*The closing Function*
f_o	*The opening Function*

References

1- Mohanty, R., U.S.M. Balaji, and A.K. Pradhan, *An Accurate Noniterative Fault-Location Technique for Low-Voltage DC Microgrid.* IEEE Transactions on Power Delivery, 2016. **31**(2): p. 475-481.

2- Nilanjan Chaudhuri, B.C., Rajat Majumder, Amirnaser Yazdani, *Multi-terminal Direct-Current Grids: Modeling, Analysis, and Control*. 2014, Wiley-IEEE Press. p. 288.

3- Fletcher, S.D.A., et al., *Optimizing the Roles of Unit and Non-unit Protection Methods Within DC Microgrids.* IEEE Transactions on Smart Grid, 2012. **3**(4): p. 2079-2087.

4- Saleh, K.A., A. Hooshyar, and E.F. El-Saadany, *Hybrid Passive-Overcurrent Relay for Detection of Faults in Low-Voltage DC Grids.* IEEE Transactions on Smart Grid, 2017. **8**(3): p. 1129-1138.

5- Emhemed, A.A.S., et al., *Validation of Fast and Selective Protection Scheme for an LVDC Distribution Network.* IEEE Transactions on Power Delivery, 2017. **32**(3): p. 1432-1440.

6- Telukunta, V., et al., *Protection challenges under bulk penetration of renewable energy resources in power systems: A review.* CSEE Journal of Power and Energy Systems, 2017. **3**(4): p. 365-379.

7- Augustine, S., et al., *Fault Current Control and Protection in a Standalone DC Microgrid Using Adaptive Droop and Current Derivative.* IEEE Journal of Emerging and Selected Topics in Power Electronics, 2020: p. 1-1.

8- Singh, B. and S. Kumar, *Distributed Incremental Adaptive Filter Controlled Grid Interactive Residential Photovoltaic-Battery Based Microgrid for Rural Electrification.* IEEE Transactions on Industry Applications, 2020. **56**(4): p. 4114-4123.

9- Kumar, S. and B. Singh, *Dual-mode control of utility interactive microgrid.* IET Renewable Power Generation, 2020. **14**(5): p. 845-855.

10- Gowtham, K., et al. *A Management of power flow for DC Microgrid with Solar and Wind Energy Sources*. in *2018 International Conference on Computer Communication and Informatics (ICCCI)*. 2018.

11- Thogaru, R.b. and A. Mitra. *Voltage Stability and Loadability Improvement of DC Microgrid Connected with Static and Dynamic Loads*. in *2019 IEEE 5th International Conference for Convergence in Technology (I2CT)*. 2019.

12- Haroun, R., et al., *Modelling and Control of Modular DC-Nanogrids Based on Loss-Free Resistors.* IEEE Access, 2020. **8**: p. 33305-33317.

13- Ul-Haq, A., et al., *Modeling and Fault Categorization in Thin-Film and Crystalline PV Arrays Through Multilayer Neural Network Algorithm.* IEEE Access, 2020. **8**: p. 102235-102255.

14- Shan, Y., et al., *Model Predictive Control of Bidirectional DC–DC Converters and AC/DC Interlinking Converters—A New Control Method for PV-Wind-Battery Microgrids.* IEEE Transactions on Sustainable Energy, 2019. **10**(4): p. 1823-1833.

15- K, J.M., et al. *Design and Simulation of Stand-alone DC Microgrid with Energy Storage System*. in *2019 IEEE International Conference on Intelligent Techniques in Control, Optimization and Signal Processing (INCOS)*. 2019.

16- Aponte-Roa, D.A., G.D.G. Cabarcas, and W.W. Weaver. *AC Vs DC Power Efficiency Comparison of a Hybrid Wind/Solar Microgrid*. in *2020 IEEE Conference on Technologies for Sustainability (SusTech)*. 2020.

17- Hasheminejad, S., et al., *Traveling-wave-based protection of parallel transmission lines using Teager energy operator and fuzzy systems.* IET Generation, Transmission & Distribution, 2016. **10**(4): p. 1067-1074.
18- Abdollahi, A. and S. Seyedtabaii. *Transmission line fault location estimation by Fourier & wavelet transforms using ANN*. in *2010 4th International Power Engineering and Optimization Conference (PEOCO)*. 2010.
19- Johnson, J.M. and A. Yadav, *Complete protection scheme for fault detection, classification and location estimation in HVDC transmission lines using support vector machines.* IET Science, Measurement & Technology, 2017. **11**(3): p. 279-287.
20- Yadav, A. and A. Swetapadma, *Enhancing the performance of transmission line directional relaying, fault classification and fault location schemes using fuzzy inference system.* IET Generation, Transmission & Distribution, 2015. **9**(6): p. 580-591.
21- Rafinia, A. and J. Moshtagh, *A new approach to fault location in three-phase underground distribution system using combination of wavelet analysis with ANN and FLS.* International Journal of Electrical Power & Energy Systems, 2014. **55**: p. 261–274.
22- Youssef, O.A.S., *Combined fuzzy-logic wavelet-based fault classification technique for power system relaying.* IEEE Transactions on Power Delivery, 2004. **19**(2): p. 582-589.
23- Feng, X., L. Qi, and J. Pan. *A novel fault location method and algorithm for DC distribution protection*. in *2016 IEEE Industry Applications Society Annual Meeting*. 2016.
24- Ananthan, S.N., et al., *Real-time fault analysis of transmission lines using wavelet multi-resolution analysis based frequency-domain approach.* IET Science, Measurement & Technology, 2016. **10**(7): p. 693-703.
25- Rathore, B. and A.G. Shaik, *Wavelet-alienation based transmission line protection scheme.* IET Generation, Transmission & Distribution, 2017. **11**(4): p. 995-1003.
26- Dhar, S., R.K. Patnaik, and P.K. Dash, *Fault Detection and Location of Photovoltaic Based DC Microgrid Using Differential Protection Strategy.* IEEE Transactions on Smart Grid, 2018. **9**(5): p. 4303-4312.
27- Fletcher, S.D.A., et al., *High-Speed Differential Protection for Smart DC Distribution Systems.* IEEE Transactions on Smart Grid, 2014. **5**(5): p. 2610-2617.
28- Park, J., et al., *DC Ring-Bus Microgrid Fault Protection and Identification of Fault Location.* IEEE Transactions on Power Delivery, 2013. **28**(4): p. 2574-2584.
29- Xu, M.M., L.Y. Xiao, and H.F. Wang. *A prony-based method of locating short-circuit fault in DC distribution system*. in *2nd IET Renewable Power Generation Conference (RPG 2013)*. 2013.
30- Park, J., *Ground Fault Detection and Location for Ungrounded DC Traction Power Systems.* IEEE Transactions on Vehicular Technology, 2015. **64**(12): p. 5667-5676.
31- Christopher, E., et al., *Fault Location in a Zonal DC Marine Power System Using Active Impedance Estimation.* IEEE Transactions on Industry Applications, 2013. **49**(2): p. 860-865.
32- Zadsar, M., M.R. Haghifam, and S.M.M. Larimi, *Approach for self-healing resilient operation of active distribution network with microgrid.* IET Generation, Transmission & Distribution, 2017. **11**(18): p. 4633-4643.
33- Jia, K., et al., *Marine Power Distribution System Fault Location Using a Portable Injection Unit.* IEEE Transactions on Power Delivery, 2015. **30**(2): p. 818-826.
34- Pradhan, A.K. and R. Mohanty. *Cable fault location in a DC microgrid using current injection technique*. in *2016 National Power Systems Conference (NPSC)*. 2016.
35- Shahrtash, S.M. and F. Haghjoo, *Instantaneous wavelet transform decomposition filter for on-line applications.* Iranian Journal of Science & Technology, Transaction B: Engineering, 2009. **33**: p. 491-510.
36- Monadi, M., et al., *Centralized Protection Strategy for Medium Voltage DC Microgrids.* IEEE Transactions on Power Delivery, 2017. **32**(1): p. 430-440.
37- Anun, M., et al., *Circular Switching Surface Technique: High-Performance Constant Power Load Stabilization for Electric Vehicle Systems.* IEEE Transactions on Power Electronics, 2015. **30**(8): p. 4560-4572.
38- Paz, F. and M. Ordonez, *An embedded impedance measurement for DC microgrids based on a Lock-In Amplifier*. 2016. 1-6.
39- Paz, F. and M. Ordonez, *High-Performance Solar MPPT Using Switching Ripple Identification Based on a Lock-In Amplifier.* IEEE Transactions on Industrial Electronics, 2016. **63**(6): p. 3595-3604.

40- Duan, J., K. Zhang, and L. Cheng, *A Novel Method of Fault Location for Single-Phase Microgrids.* IEEE Transactions on Smart Grid, 2016. **7**(2): p. 915-925.
41- Gautam, S. and S.M. Brahma, *Detection of High Impedance Fault in Power Distribution Systems Using Mathematical Morphology.* IEEE Transactions on Power Systems, 2013. **28**(2): p. 1226-1234.
42- Zhang, L.L., et al., *Morphology Singular Entropy-Based Phase Selector Using Short Data Window for Transmission Lines.* IEEE Transactions on Power Delivery, 2014. **29**(5): p. 2162-2171.
43- Namdari, F. and M. Salehi, *High-Speed Protection Scheme Based on Initial Current Traveling Wave for Transmission Lines Employing Mathematical Morphology.* IEEE Transactions on Power Delivery, 2017. **32**(1): p. 246-253.
44- Aki, H., *Demand-Side Resiliency and Electricity Continuity: Experiences and Lessons Learned in Japan.* Proceedings of the IEEE, 2017. **105**(7): p. 1443-1455.
45- Li, K., S. Zhao, and Y. Wang, *A Planar Location Method for DC Arc Faults Using Dual Radiation Detection Points and DANN.* IEEE Transactions on Instrumentation and Measurement, 2020. **69**(8): p. 5478-5487.
46- *Madeti, S.R. and S. Singh, A comprehensive study on different types of faults and detection techniques for solar photovoltaic system. Solar Energy, 2017. 158: p. 161-185.*
47- Jain, P., *et al. Fault diagnosis via PV panel-integrated power electronics. in 2016 IEEE 17th Workshop on Control and Modeling for Power Electronics (COMPEL). 2016. IEEE.*
48- Heidari, N., *et al., Impact of snow and ground interference on photovoltaic electric system performance. IEEE Journal of Photovoltaics, 2015. **5**(6): p. 1680-1685.*
49- Nguyen, X.H., *Matlab/Simulink based modeling to study effect of partial shadow on solar photovoltaic array. Environmental Systems Research, 2015. **4**(1): p. 20.*
50- Pillai, D.S., F. Blaabjerg, and N. Rajasekar, *A comparative evaluation of advanced fault detection approaches for PV systems. IEEE Journal of Photovoltaics, 2019. **9**(2): p. 513-527.*
51- Triki-Lahiani, A., A.B.-B. Abdelghani, and I. Slama-Belkhodja, *Fault detection and monitoring systems for photovoltaic installations: A review. Renewable and Sustainable Energy Reviews, 2018. **82**: p. 2680-2692.*
52- Manohar, M., E. Koley, and S. Ghosh, *Enhancing resilience of PV-fed microgrid by improved relaying and differentiating between inverter faults and distribution line faults. International Journal of Electrical Power & Energy Systems, 2019. **108**: p. 271-279.*
53- Livera, A., *et al., Recent advances in failure diagnosis techniques based on performance data analysis for grid-connected photovoltaic systems. Renewable energy, 2018. **113**: p. 126-143.*
54- Dodangeh M, Ghaffarzadeh N., *A New Fast and Accurate Fault Location and Classification Method on MTDC Microgrids Using Current Injection Technique, Traveling-Waves, Online Wavelet, and Mathematical Morphology.* IJEEE. 2020; **16**(2): p. 248-258.
55- Mellit, A., G.M. Tina, and S.A. Kalogirou, *Fault detection and diagnosis methods for photovoltaic systems: A review. Renewable and Sustainable Energy Reviews, 2018. **91**: p. 1-17.*
56- Livera, A., *et al. On-line failure diagnosis of grid-connected photovoltaic systems based on fuzzy logic. in 2018 IEEE 12th International Conference on Compatibility, Power Electronics and Power Engineering (CPE-POWERENG 2018). 2018. IEEE.*
57- Kasar, K. and P. Tapre., *A new fast detection module for short-circuit current detection in PV grid system. in 2018 2nd International Conference on Inventive Systems and Control (ICISC). 2018. IEEE.*
58- Kasemann, M., *et al., Luminescence imaging for the detection of shunts on silicon solar cells.* Progress in Photovoltaics: Research and Applications, 2008. 16(4): p. 297-305.
59- Garcia, O., J.-C. Hernandez, and F. Jurado, *Guidelines for protection against overcurrent in photovoltaic generators.* Advances in Electrical and Computer Engineering, 2012. 12(4): p. 63-70.